Article:

Langdon, G.S. orcid.org/0000-0002-0396-9787, Kriek, S. and Nurick, G.N. (2020) Influence of venting on the response of scaled aircraft luggage containers subjected to internal blast loading. International Journal of Impact Engineering, 141. 103567. ISSN 0734-743X

https://doi.org/10.1016/j.ijimpeng.2020.103567

Influence of venting on the response of scaled aircraft luggage containers subjected to internal blast loading

G.S. Langdon*, S. Kriek, G.N. Nurick

Blast Impact and Survivability Research Unit, Department of Mechanical Engineering, University of Cape Town, Cape Town, 7700. Email: Genevieve.langdon@uct.ac.za

Abstract

This paper concerns the mitigation of damage in aircraft luggage containers subjected to internal blast loading. It reports findings of experimental and computational work on the influence of venting on the blast response of scaled unit load devices. The internal geometry of the structure was based on a 1:6 scale version of the commonly used LD-3 unit load device. To simplify the problem, only the face closest to the aircraft primary structure could deform whilst the other walls were kept rigid. Small, spherical, charges of PE4 plastic explosive were detonated inside the scaled structures. The fully confined blast tests exhibited the highest permanent displacements and were the only tests to produce rupture of the target plate. Introducing venting reduced the target plate displacement significantly. Computational simulations were developed using LS-Dyna to provide additional insight into the blast loading and its interaction with the structure beyond what could be measured experimentally. Venting appeared to have no effect on the pressure peak, but it was effective at removing the late-time pressure reflections. The influence of the side venting was slightly obscured in the experiments due to boundary pulling-in effects at higher charge masses, but the simulations showed that venting from two sides was slightly more effective in reducing target plate deformation than single-sided venting. The paper demonstrates the potential benefit of using LD-3 ULDs unit load device with canvas sides (rather than solid ones) and venting lengthwise along the aircraft body to redirect the loading away from vulnerable locations.

Keywords: Blast loading; venting; aircraft structures; deformation; blast experiments; modelling

Introduction

Bombing incidents onboard aircraft have decreased significantly and air travel continues to be the safest mode of transportation [1-4]. However, bombings still happen occasionally, and it is impossible to guarantee they will not occur again, although airline security is among the strictest in the world [4]. Therefore, improving survivability following onboard explosions remains a high research priority. A possible location for explosives onboard is a luggage container. Most commercial aircraft use container-type ULDs (unit load devices) to store freight and passenger luggage in the lower deck [5]. Detonation within a ULD could cause catastrophic failure, especially if it ruptures and the blast waves impinge directly on the fuselage skin [6].

The LD-3 is a commonly used ULD as it is compatible with most wide-bodied commercial air-craft [5]. The LD-3 is approximately half the width of the cargo hold and has a diagonal side to accommodate the curvature of the aircraft body. Two LD-3 containers are installed alongside back-to-back in the lower deck of the aircraft, with several pairs of containers spaced along the length of the aircraft [5]. The diagonal side of the ULD is positioned closest to the fuselage. Rupture of this face presents a risk to the fuselage should an explosive detonation occur within the ULD. LD-3 structures are manufactured from sheet aluminium alloy which is riveted to a lightweight frame. One or two of the straight sides are sometimes replaced with canvas sheeting [5], which makes it easier to access the contents.

An internal explosion within a ULD would normally be classified as a confined blast [7]. The detonation of plastic explosive produces a blast wave that will generate multiple shock waves reverberating within the container due to the reflected pressure from the ULD walls. A rise in internal pressure is also generated by the expansion of the explosion products, producing a long duration, quasi-static load on the container, which diminishes quicker as more venting area is introduced [8-9]. In some LD-3 structures, the use of canvas sheeting allows for venting that should reduce the quasi-static pressure.

Keenan and Tancreto [8] categorised confined blasts according to a scaled venting area – which was indicative of the degree of confinement – as described by Eq. (1).

$$\zeta = \frac{A}{V^{2/3}} \quad (1)$$

Where ζ = scaled venting area, A = total venting area, and V = free volume within the container. Containers with $\zeta = 0$ are termed "fully-confined", and containers with $\zeta \leq 0.6$ and $\zeta > 0.6$ are termed "partially-confined" and "fully-vented", respectively.

Geretto et al. [10] investigated the deformation of square steel plates when blast tested with different degrees of confinement. Spheres of plastic explosive PE4 (10-70g range) were detonated at the geometric centre of the cuboidal structures, which were designed to be either fully-confined or fully-vented (with $\zeta = 1.0$). The results were compared to similar unconfined air-blast test results on square plates. For the same charge mass, the permanent midpoint displacement increased with an increasing degree of confinement.

Gatto and Krznaric [11] investigated the effect of luggage capacity and a venting area (with $\zeta = 0.840$) on the blast response of ULDs. Three different luggage capacities: 0% (empty), 50% and 75% full were compared, and the results showed that luggage significantly reduced the pressure magnitudes (for example, 75% luggage capacity reduced the initial peak pressures by 99%). Additional tests investigated the effect of venting, by replacing the steel door with a plywood door (venting available only after the door failed) and no door (venting immediately available). The venting area only reduced the quasi-static pressure, with immediate venting allowing the quickest return to atmospheric pressure after detonation.

This paper reports on the influence of venting on the response of internally blast-loaded scaled LD-3 structures. A scaled model, with representative geometry of a LD-3 and various venting configurations, was subjected to blast loading. The transient and permanent deformation of the diagonal side was used as the performance measure. The computational simulations provided additional insight into the pressure evolution that could not be determined experimentally. Although it should be noted that the effect of luggage within the containers has not been addressed in the current work, past research has shown that luggage reduced the blast loading and container damage [11], hence it is assumed that detonations within empty containers is a worst-case scenario. The findings presented herein should prove useful to blast engineers seeking mitigation solutions onboard aircraft.

1. Air-blast experimentation

1.1 Test structure

The test structure was manufactured at 1:6 scale, based on the internal dimensions of the LD-3. The 1:6 scale was the best compromise between having sufficient internal free volume (accurate explosive positioning inside the structure) and low mass (easy handling). The real LD-3 is manufactured using a lightweight tubular aluminium alloy frame and thin aluminium sheeting riveted along the edges [5]. As shown in Figure 1, most of the tested structure comprised 20 mm thick steel walls (to allow for a rigid assumption) with one deformable AA5754h22 aluminium alloy target plate. The target plate was clamped to the diagonal side, as shown in Figure 1. The thick walls were assumed to remain rigid during the blast testing, allowing multiple blast tests to be performed within the single box. The exposed area of the target plate was 255 mm × 117 mm.

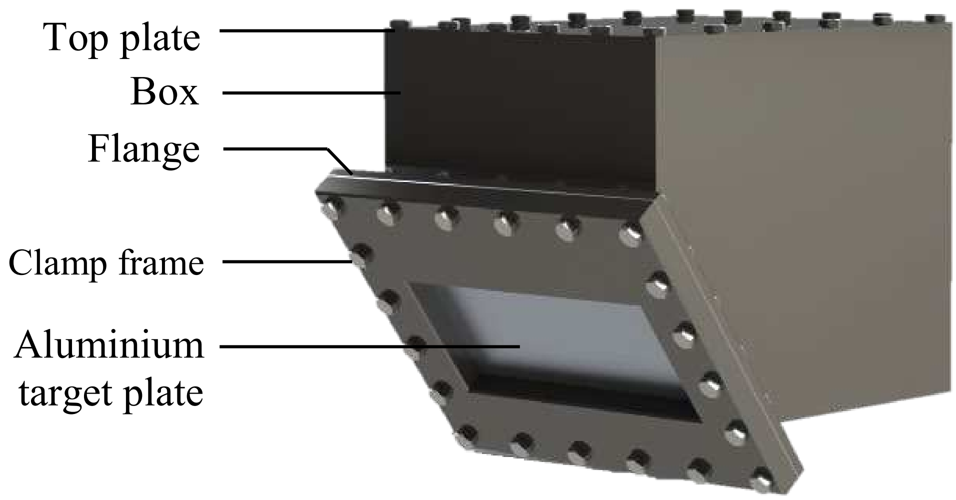

Figure 1: Schematic showing the structure used in the scaled experiments, based on the internal geometry of a 1:6 scaled LD-3

1.2 Internal confined blast test method

Bare, spherical, plastic explosive PE4 charges were detonated inside the empty structure to produce the internal blast loading. A polystyrene bridge was used to position the charges at the volumetric centre, and perpendicular to the geometric centre of the AA5754h22 aluminium alloy target plate. Hence, the stand-off distance (SOD), defined as the distance from the charge centre to the target plate surface, was kept constant at 163 mm. The charge mass was varied between 10g and 25g to obtain a range of responses in the deformable target plates. This would be equivalent to a full-scale charge mass range of 1.9 kg to 5.9 kg. Three venting configurations were tested for the internal blast detonations: (1) no venting (fully confined), (2) single-sided venting (ζ = 0.7) and (3) double-sided venting (ζ = 1.4). The test arrangement for the fully-confined tests is shown in Figure 2. Following the experiments, all the target plates were scanned using a 3D scanner to obtain surface plots of the deformed rear surface.

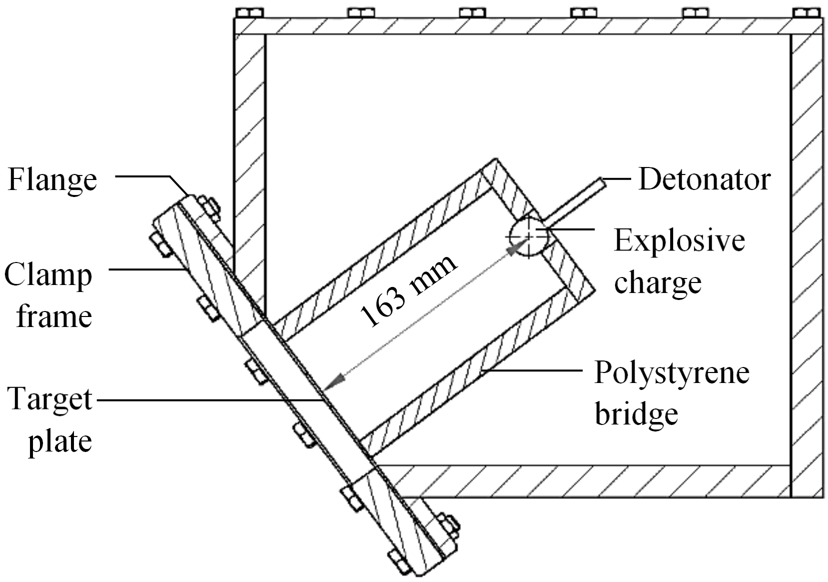

Figure 2: Schematic section view of the load setup for confined blast tests.

1.3 Unconfined blast test method

The unconfined blast tests were performed on the same batch of AA5754h22 target plates using the same boundary conditions and spherical PE4 charges. The tests were performed on a pendulum fitted with a pair of IDT vision NR4 S3 high-speed monochrome cameras which captured the transient blast response of the target plate. The cameras were rail mounted and assumed not to move independently from each other. The field of view was focussed on the central strip of the plates and the cameras had an included angle of approximately 30°. The charge mass was varied from 10g to 25g with repeat tests performed in the 10-17g range.

1.4 Transient response measurements during the unconfined tests

Tests were filmed at 16 000 fps, over a 1024 pix x 180 pix region of interest, with an exposure time of 31 μs The cameras were triggered using a custom-made TTL circuit activated by the explosive detonation. Each camera was focused on the central strip across the length of the target plate. The equipment was enclosed by a pair of shrouds which protected the cameras from the detonation flash and combustion products, shown in Figure 3. Dantec Dynamics Istra 4D DIC software was used to extract the images and measurements from the camera system. LED lights were used to illuminate the rear surface of the target plate which was speckled with a random pattern. The stereo-imaging system was calibrated prior to testing by taking multiple images of a checkerboard patterned calibration target at different positions using both cameras. The DIC software calculated system parameters and calibration values for use during post-processing.

During post-processing, the specimen deformation was determined by tracking the movement of the speckle pattern using a correlation algorithm to minimise the errors. Data was extracted along a centre line indicated on the plate using two markers, and mid-point displacement was calculated. Further details on this method are available in reference [12].

Figure 3: Photographs of unconfined blast rig setup showing the target plate (left) and the high-speed camera system inside the shroud (right).

2. Experimental Results

2.1 Unconfined blast tests: permanent deformation

Thirteen unconfined blast tests were performed in total, with six of those tests providing transient response measurements. A summary of the unconfined blast tests results is given in Table 1. The peak transient displacements are 1-2 plate thicknesses greater than the permanent mid-point displacements, which was expected. The target plates exhibited large plastic deformation with classical yield line formation that is typical of impulsively loaded rectangular panels with clamped boundary conditions. The action of membrane action becomes more evident as charge mass increased, indicated by the rounding of the profile between the plastic hinge lines.

Some typical contour plots of the permanently deformed profiles are shown in Figure 4. Each band represents a 1mm step in displacement. The yield lines extending from the corners towards the plate centre are more evident at higher charge masses. No plate rupture or significant material thinning were evident in the plates for the tested charge mass range. Photograph of typical deformed plates tested at 25g are shown in Figure 5, including the unconfined 25g detonation in Figure 5a.

Table 1: Summary of unconfined blast test results

Test number	**Charge mass (g)**	**Peak midpoint displacement (mm)**	**Perm. midpoint displacement (mm)**	**Maximum permanent displacement (mm)**
DIC3	10	9.84	7.22	7.88
DIC10	10	9.34	5.73	6.58
DIC1	12	-	7.11	6.73
UC1	12	-	7.61	7.81
DIC4	12	11.19	8.50	9.16
DIC5	12	9.43	6.32	7.14
DIC2	15	-	12.36	12.61
DIC6	15	15.41	12.89	13.06
DIC9	17	13.67	10.65	11.58
DIC7	17	-	10.67	11.13
DIC8	17	-	13.85	13.92
UC2	20	-	11.10	11.86
UC3	25	-	14.89	14.92

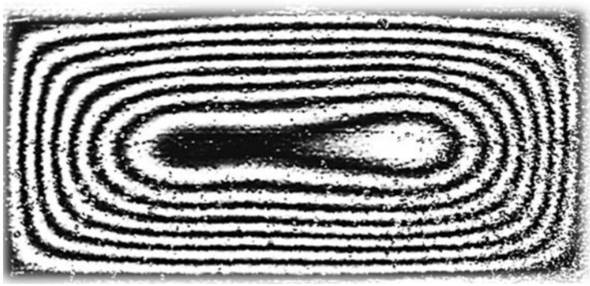 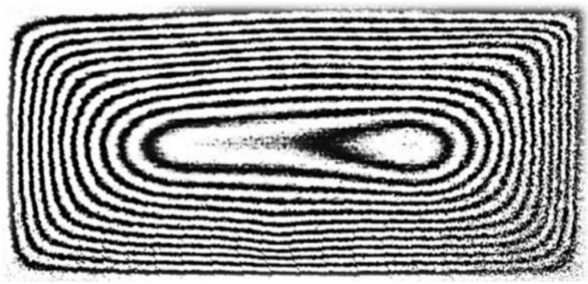

(a) **(b)**

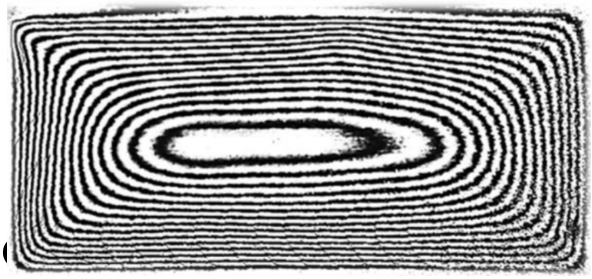

Figure 4: Selected permanent displacement contour maps from unconfined test target panels (a) UC1, 12g detonation (b) UC2, 20g detonation (c) UC3, 25g detonation

A graph of permanent mid-point displacement versus charge mass is shown in Figure 6. There is a general trend of increasing mid-point displacement with increasing charge mass, although some of the results are outside the expected trend. Two reasons are apparent for the observed deviations. Firstly, small asymmetries in the displacement profiles were measured, with the difference between the maximum permanent displacement and the mid-point permanent displacement being less than 1 mm. However, for the 10g and 12g tests, an asymmetry of nearly 0.9 mm was observed in two tests represented a high percentage (11-13%) of the final displacement. This meant the permanent displacement measurements were slightly lower than anticipated. Secondly, there was some localised deformation (pulling-in) observed along the boundary edge in three tests, as indicated in Figure 6. Pulling in of the boundary is known to increase the mid-point displacement and delay tearing failures [13-14]. When these tests are excluded, a linear trend line with a R^2 coefficient of 0.96 was fitted through the data.

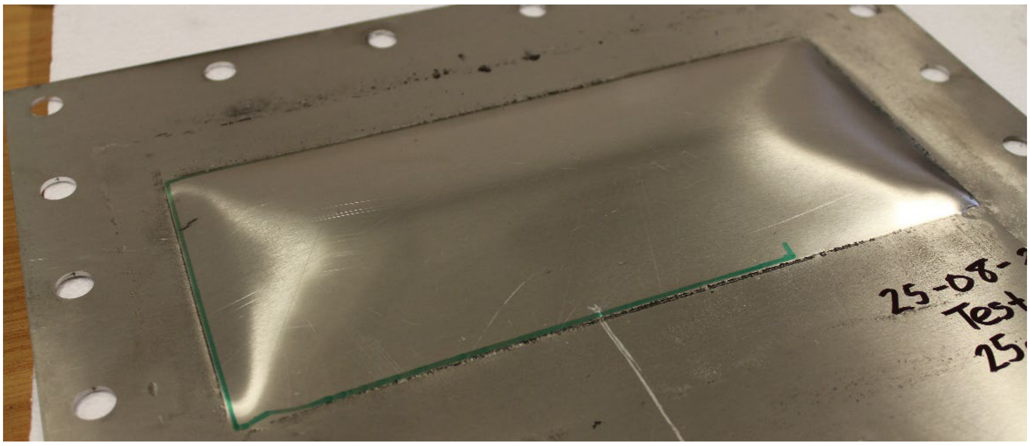

(a)

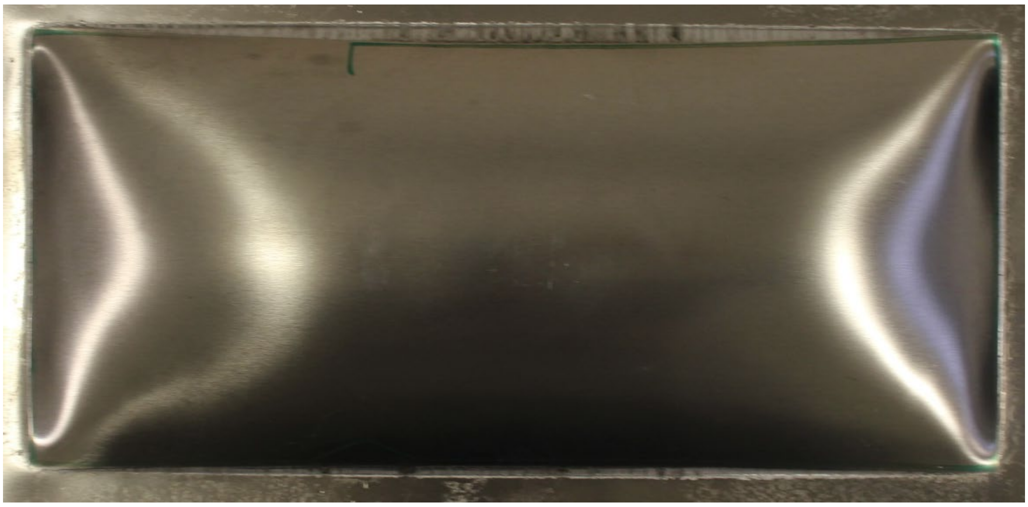

(b)

(c)

Figure 5: Photographs of selected target plates (a) unconfined UC3, 25g, oblique view (b) double-sided venting (ζ = 1.4), 25g, top view (c) fully confined, 20g, top view

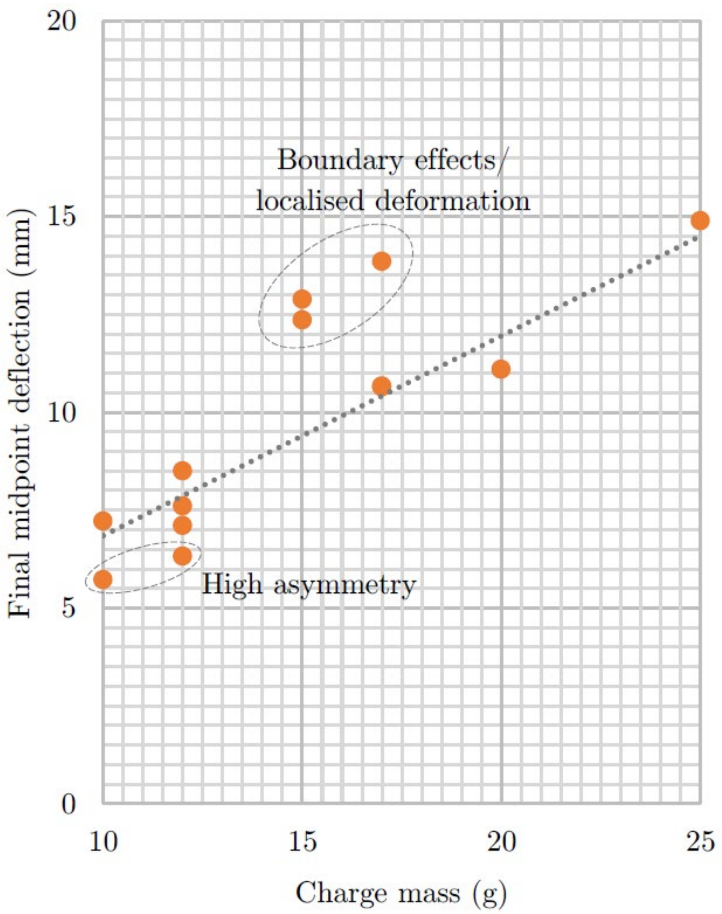

Figure 6: Graph of permanent mid-point displacement versus charge mass, with inconsistent tests highlighted

2.2 Unconfined blast tests: transient response

The transient mid-point displacement-time histories obtained from the unconfined blast experiments (red and blue lines) for the 10g, 12g and 17g detonations are shown in Figures 7a, 7b and 8 respectively. Although the numerical simulation results are also presented in Figure 7 and 8, these will only be discussed in section 4, after the presentation of the model development. This section will only describe the experimentally measured transient response. The 15g tests were excluded because of the localised boundary effects. The two 10g and 12g detonations, shown in Figure 7, gave very repeatable responses. For all charge masses, the target plates began to move 100μs after detonation and peak deflection was reached just before 400 μs. The panels recovered elastically after peak and oscillated about a permanent displacement. The permanent mid-point displacement obtained from an average of the longer-time oscillations captured from the camera images agreed well with the post-test manual measurements.

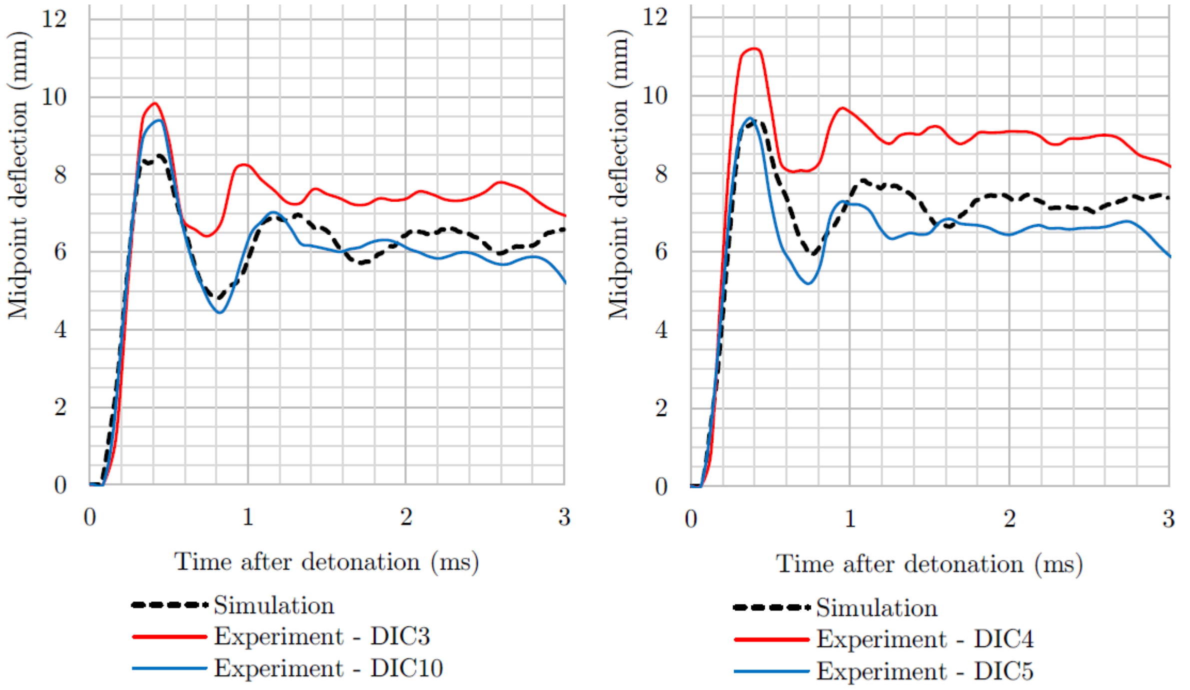

(a) (b)

Figure 7: Graph of transient mid-point displacement versus time showing experimental (blue, red) and simulation (black) results (a) 10g (b) 12g

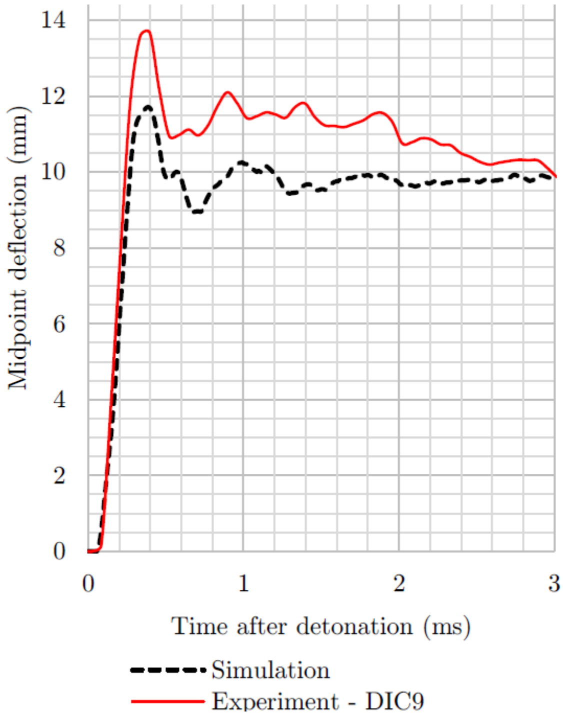

Figure 8: Graph of transient mid-point displacement versus time for a 17g detonation, showing experimental (red) and simulation (black) results

The transient evolution of the target plate profile across the long-wise mid-line (255 mm long) is shown in Figure 9 for a 12g unconfined detonation (DIC5), at various times. The deformation near to the clamped boundary was not captured by the cameras due to obscuration by the clamp frame. Similar profiles were obtained for all tests with transient data capture.

The target plate movement initiated in the centre. The inertia imparted to the target plate from the blast loading caused a rapid rise in deformation across the profile during the first 200µs of response. The effect of the clamped boundary edge constraining the deformation and the forming of yield line occurs thereafter, causing the flattening of the profile across the middle third of the target plate, as seen in Figure 9. The peak displacement, indicated by the red lines in Figures 9a and 9b, was reached after approximately 375 µs. The profile shapes captured after 500 µs matched those of the final profile, shown in black, in Figure 9b. The elastic rebound caused a small decrease in displacement but did not substantially affect the shape.

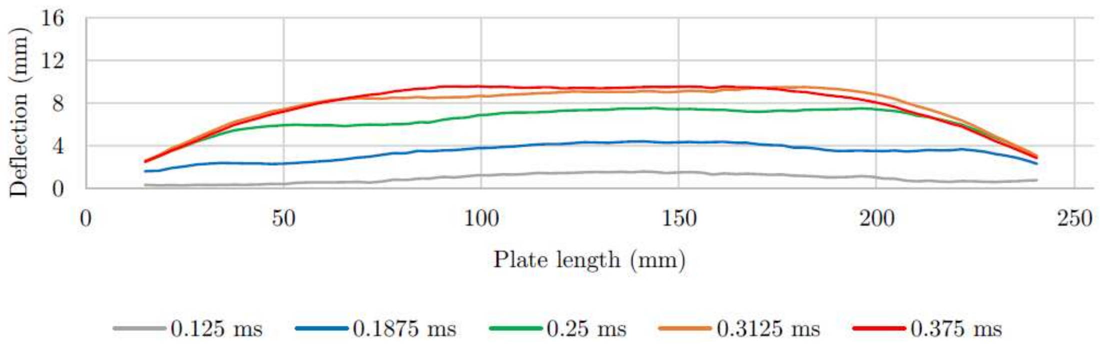

(a)

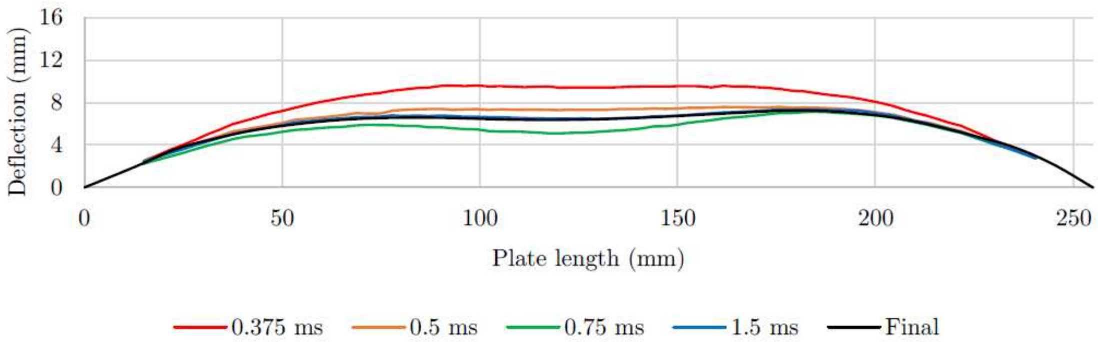

(b)

Figure 9: Graphs showing the evolution of the lengthwise deformed profile, 12g detonation (unconfined, DIC5) (a) 0-375 μs (b) post-peak response (after 375 μs)

2.3 Influence of venting and confinement

Thirteen additional blast tests were performed to investigate the influence of confinement on the response of the target plate. Table 2 is a summary of the fully confined, single-sided venting and double-sided venting blast test results. The deformation mode was large plastic deformation with classical yield line formation, accompanied by some membrane action that rounded the profile, like the unconfined tests. The maximum and mid-point permanent displacements were similar, with small variations of up to 1 mm observed in some experiments and no differences in others. Plate rupture extending along the entire boundary edge was observed in the fully confined (that is, no venting) test at 20g. A photograph of the target plate is shown in Figure 5c. No other plate ruptures were observed in the vented tests up to a charge mass of 25g.

Table 2: Summary of the blast tests using confinement and venting

Venting type	Test number	Charge mass (g)	Permanent midpoint displacement (mm)	Maximum permanent displacement (mm)
No venting: fully confined	FC3	10	13.67	13.67
	FC2	12	16.34	16.34
	FC4	15	17.01	17.01
	FC5	17	17.25	17.25
	FC1	20	Rupture	Rupture
Single-sided venting	FV(0.7)2	10	11.51	11.66
	FV(0.7)1	15	15.89	15.89
	FV(0.7)3	20	17.84	18.77
	FV(0.7)4	25	23.24	23.24
Double-sided	FV(1.4)1	10	11.09	11.13
	FV(1.4)2	15	15.42	16.06

venting	FV(1.4)3	20	19.03	19.25
	FV(1.4)4	25	19.67	20.08

A graph of permanent midpoint displacement versus charge mass for all confinement types is shown in Figure 10. The fully confined tests caused the largest displacements in the target plates while the unconfined tests produced the lowest displacements. The single-sided and double-sided venting are difficult to distinguish from each other but have displacements that are lower than the fully confined configuration. This highlights the potential of an open-sided LD-3 for mitigating the effects of the blast on the primary framework of an aircraft, especially considering the target plate rupture caused by the fully confined 20g detonation.

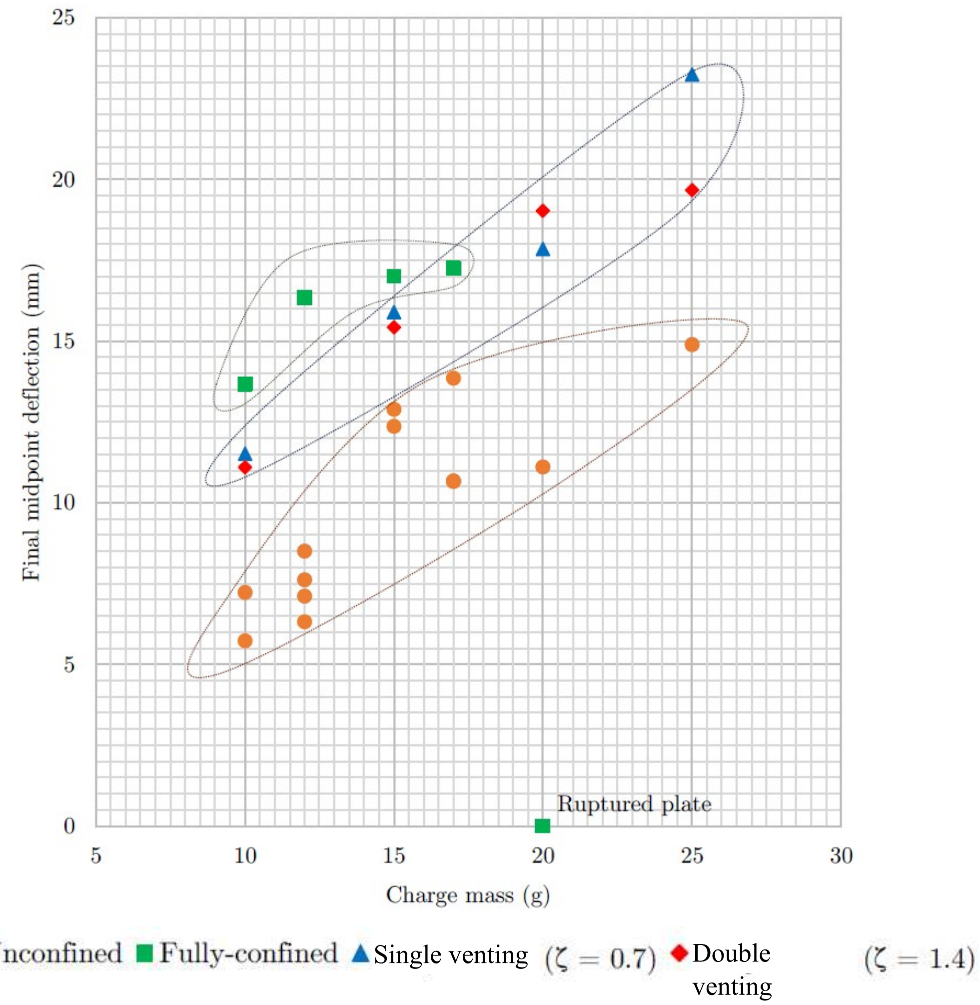

Figure 10: Graph of permanent midpoint displacement versus charge mass, showing the effect of confinement and venting

Contour plots of the permanent deformed profiles for the four test conditions at 15g are shown in Figure 11. As before, the yield lines along the diagonals are indicated by the closeness of the contour lines. There is some flattening of the profile evident in the central region, except for the plate with double venting, which also exhibited some localized irregular deformation near the bottom edge (circled in red). However, the final mid-point displacement magnitudes do not appear affected by the minor asymmetry present in the double-sided vented test. The experiments showed little difference between single-sided and double-sided venting in the shape of the deformed profiles or the magnitude of the final displacement.

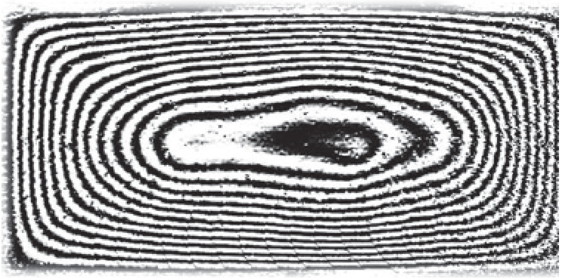
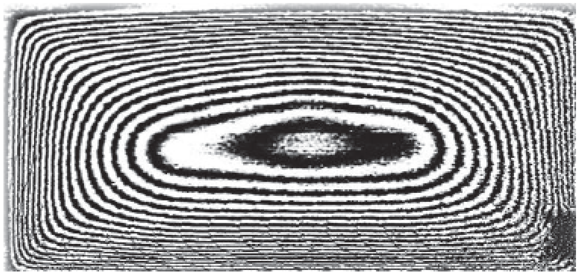

(a) Unconfined (b) Fully confined

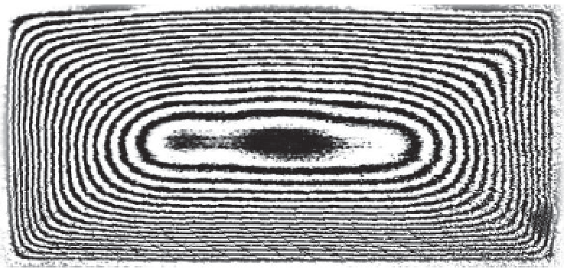
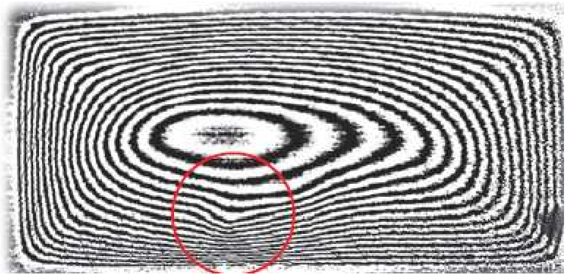

(c) Single venting ($\zeta = 0.7$) (d) Double venting ($\zeta = 1.4$)

Figure 11: Permanent displacement contour maps of the target plates, 15g tests

3. Computational simulation development

Computational simulations were developed for each of the experimental conditions using the LS DYNA® commercial software. The target plate, clamp frame and explosive were modelled using the Multi Material Arbitrary Lagrange Eulerian (MMALE) Fluid Structure Interaction (FSI) approach in LS-Dyna. Half-symmetry was used in the fully-confined, double-sided venting and unconfined models to improve the computation time. A full model was required for the single-sided venting simulation. The four models are shown in Figure 12. Mesh dependency studies were performed to determine the sizes of the air, target plate and Ld-3 structure meshes and ensure that leakage of the explosive material through the plate did not occur.

Much of the CPU time was spent finding convergence for the air mesh solution at each time step, so once the blast pressure had diminished to inconsequential levels, the air mesh was removed from the simulation. This “pressure cut-off” time was first determined for each confinement type by examining the pressure-time histories and their effect on the target plate response. To reduce the computational run-time, each simulation was run in two stages: the first was the loading stage which terminated at the pressure cut-off time. The second was an unloading phase, where a restart analysis was performed by inputting the loading conditions from the first stage and deleting the air mesh and FSI constraints. The pressure cut-off times were: 200 µs (unconfined), 700 µs (fully confined) and 400 µs for the single-sided and double-sided venting.

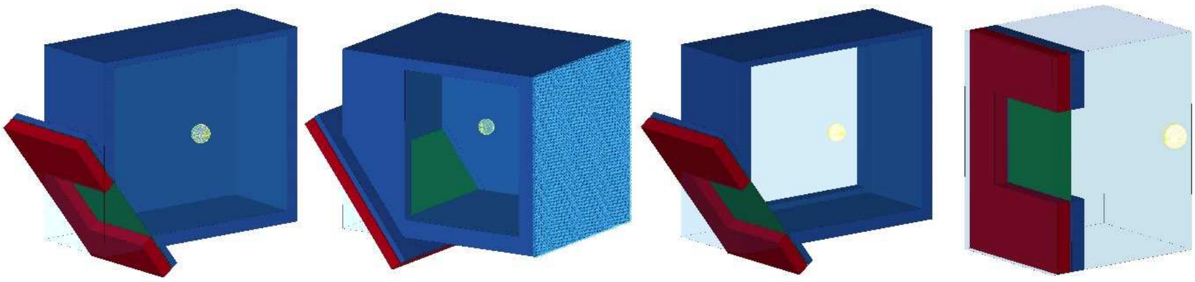

(a) (b) (c) (d)

Figure 12: Numerical blast models for (a) fully-confined, (b) single venting (ζ = 0.7), (c) double venting (ζ = 1.4) (d) unconfined blasts.

3.1 Air and explosive modelling

The air domain was modelled using 3D eight-node solid brick elements with a unity aspect ratio and an element length of 2 mm. A multi-material arbitrary Langrangian-Eulerian (MMALE) element formulation was used to model the air and explosive. Hourglass control of the solid elements was implemented using the Flanagan-Belytschko viscous form with exact volume integration.

The air was modelled as a null material obeying the ideal-gas relation. The properties (gas constant (R), specific heat ratio (γ), initial density (ρ_0) and initial internal energy per unit volume (E_0)) are listed in Table 3 and were obtained from reference [15]. The explosive was modelled using the JWL equation of state (EOS) and the high-explosive-burn material model. The material-specific EOS parameters include pressure terms (A, B) and non-dimensional terms (R_1, R_2, ω). The detonation parameters include the initial detonation energy per unit volume (E_0), detonation velocity (D), the Chapman-Jouguet pressure (P_{CJ}) and the initial density of the explosive (ρ_0). These parameters are listed in Table 4 and were obtained from reference [16]. It is assumed that PE4 and C4 properties can be used interchangeably, following the modelling approach of previous work [10, 12].

Table 3: Properties of air used in the LS-Dyna simulations [15]

R (kJ/kg · K)	γ	ρ_0 (kg/m^3)	E_0 (kJ/m^3)
0.2870	1.400	1.184	253.3

Table 4: Properties of explosive used in simulations [16]

Equation of state parameters					Detonation parameters			
A (MPa)	B (MPa)	R_1	R_2	ω	E_0 (MPa · m^3/m^3)	D (m/s)	P_{CJ} (MPa)	ρ_0 (kg/m^3)
609770	12950	4.5	1.4	0.25	9000	8193	28000	1601

3.2 Target plate modelling

The thin target plate was modelled using 2D four-node quadrilateral shell elements with an element length of 2 mm. The material definition was described by the Johnson-Cook material model [17]. The model constitutively defines the von Mises equivalent flow stress (σ_f) of a metal in terms of plastic strain (ε_p), strain rate ($\dot{\varepsilon}$) and temperature (T), as described in Eq. (2).

$$\sigma_f = \left[A + B\left(\varepsilon_p\right)^n\right] \times [1 + C\ln(\dot{\varepsilon}^*)] \times [1 - (T^*)^m] \quad (2)$$

Where the homologous strain rate and temperature are defined as $\dot{\varepsilon}^* = \dot{\varepsilon}/\dot{\varepsilon}_0$ and $T^* = (T - T_r)/(T - T_m)$, respectively, and A = material yield stress, B = strain hardening coefficient, n = strain hardening exponent, C = strain-rate sensitivity coefficient, m = thermal sensitivity exponent, $\dot{\varepsilon}_0$ = reference strain rate, T_r = reference temperature and T_m =

melt temperature.

The strain-rate and thermal sensitivity parameters were obtained from published literature [12, 18-19]. The other properties of AA5754h22 were obtained from quasi-static tensile tests following the ASTM E8 standard [20]. The tensile tests were performed in both the rolling and transverse to roll directions, at a strain rate of 3.33 x 10^{-4} s^{-1}. The material was slightly sensitive to roll direction, so the tensile tests were simulated using the implicit solver within LS-Dyna to find the Johnson-Cook parameters that best represented the behavior. Further details are available in reference [21]. The fitted parameters are given in Table 5.

Table 5: Properties of AA5754h22 used in numerical simulations

Aluminium AA5754h22 [12, 18-19]										
ρ (kg/m^3)	G (GPa)	E (GPa)	ν	T_m (K)	C_p (kJ/kg $\cdot$ K)	A (MPa)	B (MPa)	n	C	m
2700	27.0	68.0	0.3	600	0.900	160.5	339.8	0.5206	0.003	2.52

3.3 LD-3 box and clamp frame modelling

The sides of the LD-3 structure and the clamping frame were modelled using three-dimensional, eight-node solid brick elements. A 2 mm element length and unity aspect ratio were used. These steel members were modelled using an elastic formulation with assumed properties of density (7850 kg/m^3), Young's modulus (210 GPa) and poisson's ratio (0.3). A penalty coupling technique was implemented to enforce the fluid-structure interaction between the Lagrangian (structural components) and solid (air and explosive) meshes. A 2 × 2 coupling-point distribution was defined across each Lagrangian element to enforce the interaction and prevent leakage.

The simulations captured the first 3 ms of the plate response following detonation. Contact between the target plate and clamping structures was maintained by implementing an automatic surface-to-surface card to ensure representative clamped boundary conditions were simulated. The surface contact was able to restrict the plate motion, removing the need to model the clamp bolt arrangement, since no material failure was anticipated. Detonations above 20g PE4 in the fully confined structures were not simulated as tearing was observed at 20g in the experiments.

4. Discussion

4.1 Estimates of peak pressure

To ensure that the blast wave modelling gave sensible results, the simulated peak pressure from the centre of the deformable plate was compared to empirically based estimated from literature [22-23]. Brode [22] proposed a simple closed-form solution to estimate the peak overpressure due to the detonation of a sphere of plastic explosive when the over pressure is larger than 10 bar, for far-field loading conditions. This expression is given in Eq. (3):

$$p_{peak} = \frac{6.7}{Z^3} + 1 \tag{3}$$

Where p_{peak} is the peak pressure measured in bar and Z is the Hopkinson-Cranz scaled distance Z, where $Z = \frac{R}{W^{1/3}}$ and R = stand-off distance (in m) and W is the TNT equivalent mass of explosive (in kg)

Another expression for peak overpressure, this time in kPa, was employed by Mills [23], given in Eq. (4):

$$p_{peak} = \frac{1772}{Z^3} - \frac{114}{Z^2} + \frac{108}{Z} \tag{4}$$

Using a 20g PE4 detonation at a SOD of 163mm, which is typical for the testing reported herein, and a TNT equivalence for PE4 of 1.2, Eq. (3) estimates the peak overpressure of 3.8 MPa while Eq. (4) predicts a larger overpressure of 9.65 MPa. A peak pressure of 4.3 MPa was observed in the computational simulations for the 20g PE4 detonation in the unconfined case, which is between the two empirical estimates, but closer to Eq. (3). This gives confidence that LS-Dyna is correctly modelling the development of the blast wave and that the parameters assumed in Tables 3 and 4 are reasonable.

4.2 Comparisons of numerical simulations and experimental measurements

A graph of simulated versus experimentally obtained permanent mid-point displacement is shown in Figure 13. The dotted line would indicate perfect correlation. The predicted permanent mid-point displacements were slightly lower than the experimentally obtained values for all test configurations, with the best agreement obtained for the unconfined tests. The target plates, particularly those from the confined blast models, exhibited boundary pull-in. This type of failure was noticeable at the top and bottom edges of the target plate; only minor boundary pull-in occurred along the shorter plate sides. Although the models were able to capture boundary pull-in, the absence of the clamping bolts in the simulations resulted in a more uniform boundary failure than that observed in the experimental blasts. In-plane displacement of material clamped along a boundary edge increases out of plane displacements and delays the onset of tearing [13-14]. It is evident in some of the experiments (noticeable particularly in the bolt-hole elongation at high charge masses). It may also be that the materials response of the aluminium alloy at high strain rates under blast conditions deviate slightly from the published data used in the material models, thus resulting in some slight underpredictions for all the simulated deflections.

Comparisons between the transient response of the target plates from simulations and the unconfined experiments are shown in Figures 7 and 8. All qualitative aspects of the transient mid-point displacement response are well captured by the simulations, namely the initial rise in displacement, followed by a rebound and elastic oscillations. The two 10g and 12g detonations, shown in Figure 7a and 7b, gave very repeatable but not identical responses experimentally. The simulated peak displacements (indicated by the black lines in Figure 7) are slightly lower than the experimental ones in some cases, but occur at the same point in the time history.

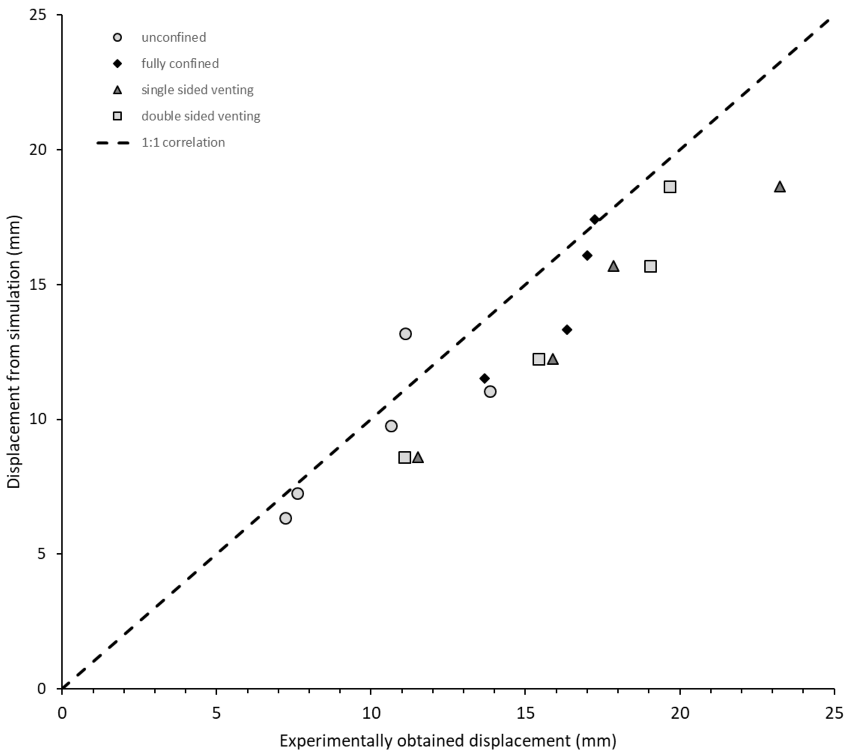

Figure 13: Graph of permanent mid-point displacement from simulations versus experimentally obtained counterparts

When the deformed profile shape was compared, there was good agreement between the experimental and simulated midline profiles for the singly-vented (ζ = 0.7) and unconfined blasts, and slightly poorer agreement between the fully-confined and all the double venting (ζ = 1.4) blasts. To illustrate the correspondence, Figure 14 shows the permanently deformed midline profiles obtained from the 10-17g detonations in the fully-confined arrangement. The red lines indicate experimental measurements while the dotted lines show the simulation results. Slight asymmetries in the experimental deformation are evident in the 12g detonation and the underprediction in permanent deflection is illustrated at low charge masses.

Figure 14: Graphs comparing the permanently deformed plate profiles across the plate midlines obtained for the confined detonations (experiments = red; simulations = black; lines are offset to distinguish between charge masses)

A graph of mid-point displacement versus charge mass obtained from simulations is shown in Figure 15 for the four configurations. The effects of confinement are even more apparent in the simulations than in the experiments, because the boundary pulling-in phenomena does not obscure the differences. Linear trends of increasing displacement with increasing charge mass are apparent within a test configuration. Interestingly, the simulated displacements are consistently lower for double-sided venting than for single-sided venting, yet this distinction was not seen in the experiments. Single-sided venting reduced the displacement of the target place by approximately 10%, and double-sided venting reduced the displacement by up to 23% when compared to the fully confined case.

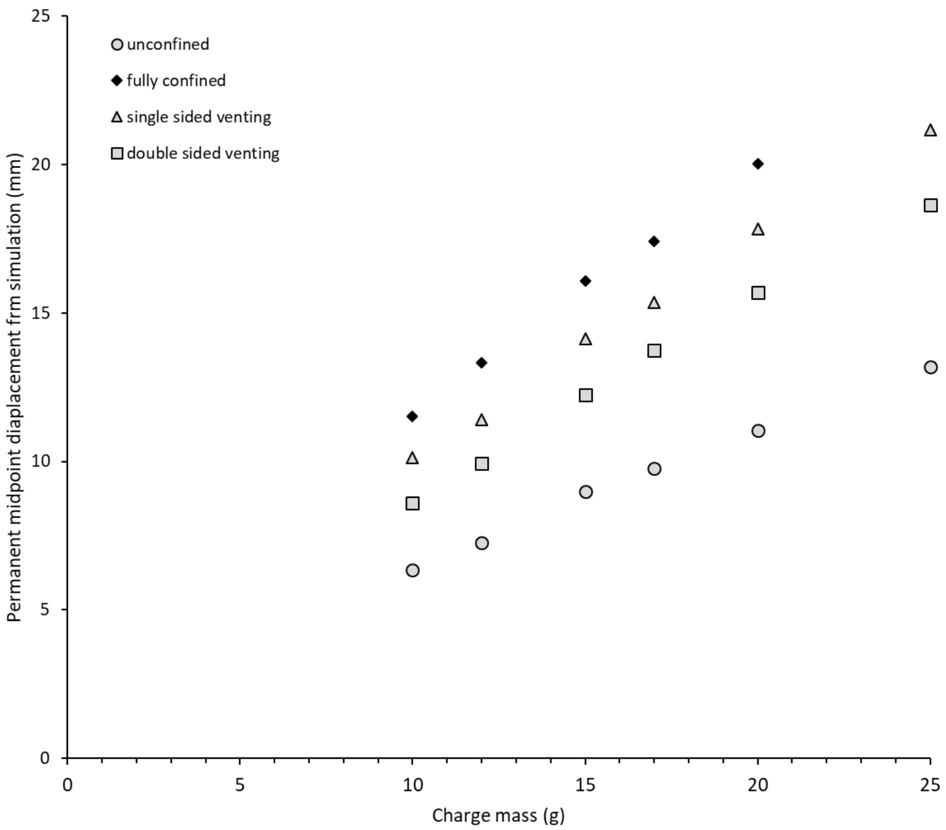

Figure 15: Graph of permanent mid-point displacement from simulations versus charge mass, showing the influence of confinement and venting

4.3 Pressure-time histories

As pressure measurements were not undertaken during the experiments, the simulations were used to gain additional insight into the influence of confinement on the loading of the target plate. The pressure at the mid-point of the target was plotted for each venting configuration, and the simulated pressure-time histories are shown in Figure 16. As expected, increasing charge mass resulted in larger peak pressures. Of greater interest is the effect of structural confinement on the initial peak pressure. The simulations indicate that the initial peak pressure increased by a factor of 3 for all arrangements with confinement (regardless of venting configuration) when compared to the unconfined configuration.

The unconfined blast loading decayed back to ambient within 150-200 μs of detonation (shown in Figure 16a). The addition of confinement caused lower magnitude pressure spikes to impinge upon the target plate subsequent to the initial pressure peak. These spikes resulted from multiple shock reflections from the rigid internal walls of the LD-3 structure. The singly-sided venting configuration exhibited a late time (around 340-380 μs after detonation) small reverberating pressure which was not present in the double-sided venting simulations, and a slightly lower rate of decay from peak pressure. The fully confined condition exhibited higher levels of pressure that continued to impinge on the target plate after 600 μs. No results are presented beyond the pressure cut-off time of 700 μs, but initial simulations showed that increasing the cut-off time to 1000 μs did not influence the final displacement of the target plate, so the late time small pressure reverberations still present in the structure after 600 μs were assumed to be insignificant. The simulations confirmed that venting had no effect on the peak pressure but was effective at removing the late-time pressure reflections that occur within the fully-confined structures. This is consistent with previous studies [8, 11].

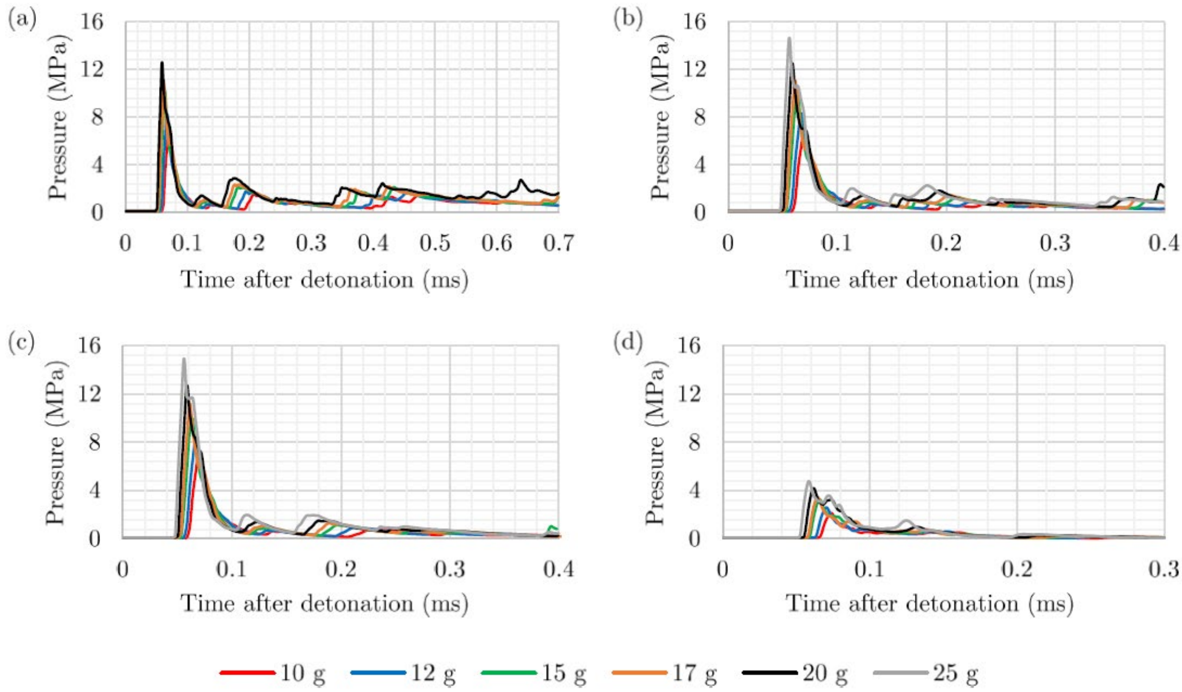

Figure 16: Simulated pressure-time histories at the target plate centre (a) fully confined (no venting), (b) single-sided venting, (c) double-sided venting, (d) unconfined.

4.4 Blast wave development and interaction

Figures 17 to 19 show the simulated blast pressure wave development for three of the confinement types subjected to a 15g charge detonation. A spherical blast wave propagated radially from the charge centre for the first 40 μs, as shown in the first two images of Figures 17 to 19. This is due to the development of the detonation wave transferred to air being a function of the charge shape and not being influenced by the confinement geometry until the blast wave begins to interact with the walls of the container.

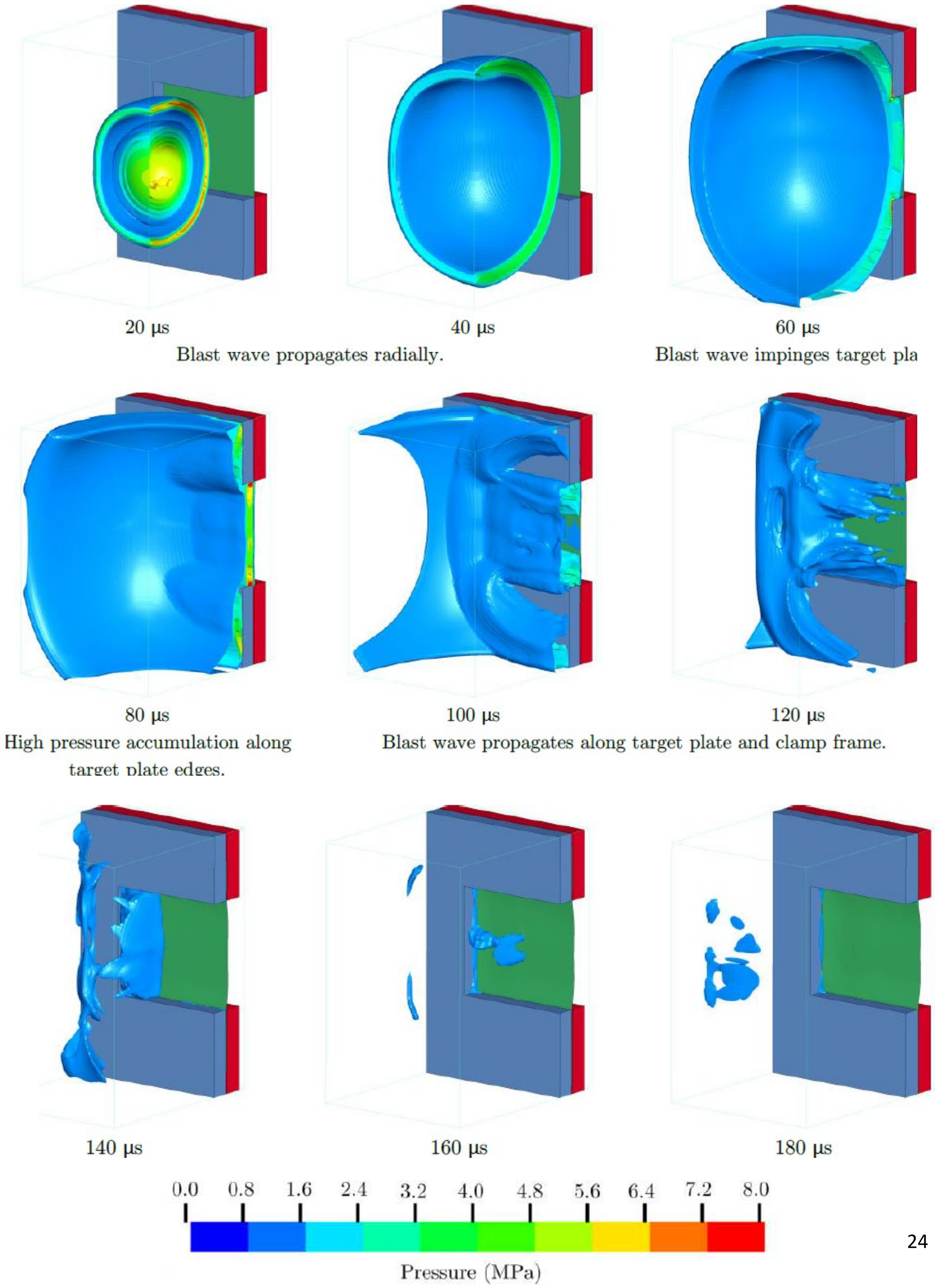

Figure 17: Simulated blast wave evolution for a 15g detonation for the unconfined test arrangement

For the unconfined case, the blast wave continued to expand radially until it impinged on the target plate, shown in the pressure contour plot at 60 μs in Figure 17. Some pressure recirculation along the target plate clamped boundary edge was evident after 80 μs, causing a small high-pressure zone to accumulate along the target plate edge. At 100 μs, the blast wave is shown to propagate along both the target plate and then across the clamp frame (120 μs), until after 160-180 μs the pressure has propagated away from the target plate and out of the air domain.

The fully confined case, shown in Figure 18, had the same pressure development as the unconfined test for the first 40 μs, and differed only once the pressure waves interacted with the confinement walls, as shown at 60 μs in Figure 18. High pressure reflections from the top and bottom walls, as well as the reflected wave from the target plate, are evident after 60 μs.

High pressures accumulated along the target plate walls, as before, after 80 μs. Blast wave reflections from the vertical walls (particularly the rear face and the vertical region above the target plate) are also exhibited. The pressure reflections from the walls caused much higher target plate pressure magnitudes between 50 μs and 80 μs. This was evident when comparing Figures 17 and 18 at this time increment and was also observed from the pressure-time history graphs shown in Figure 16. The peak pressures at the corners of the plates occurred after approximately 80 μs to 100 μs, and were typically 25 % to 30% lower in the top corner than in the bottom corner due to the internal geometry of the ULD. The time to peak pressure in the corners decreased with increasing charge mass, which was similar to the trend for peak pressure time for the mid-point of the target plate in Figure 16.

The pressure reflections within the fully confined ULD box increased the loading time, as regions of high pressure developed in the box corners due to recirculation effects (after 100 μs), shown in Figure 18. After 200 μs, the reflected blast waves returned to the centre of the ULD. For the next 300 μs, there was a complex interaction of internally reflected pressure waves accompanied by quasi-static pressure accumulation.

Figure 19 shows the development of blast waves within a single vented ULD subjected to a 15g detonation. As the single vented case was not symmetric, the full box was modelled. Unfortunately, this meant the box walls obscured some of the pressure contour plots in Figure 19, but the general development path can still be identified. As before, the differences between the singly vented and unconfined cases only became evident between 40 and 60 µs, as the pressure interacted with the ULD walls.

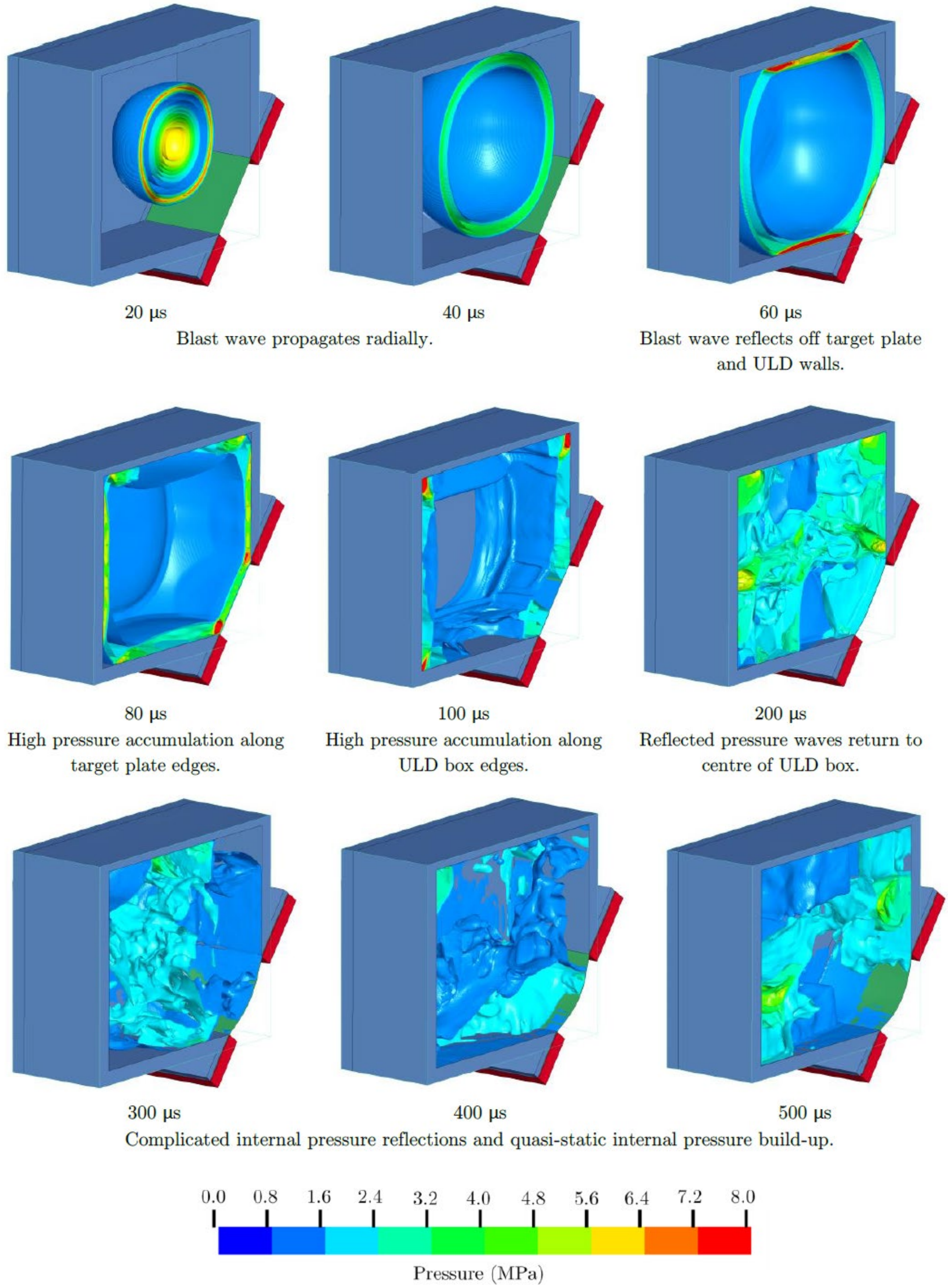

Figure 18: Simulated blast wave evolution for a 15g detonation for the fully confined test arrangement

At 60 μs, the pressure had started venting out of the open side, although this did not significantly reduce the pressure applied to the target plate until after 100 μs when compared to the fully confined case shown in Figure 18, meaning that the target plate pressure-time histories for the first 100 μs resembled the fully confined case rather than the unconfined one, confirmed by the histories at the target plate centre shown in Figure 16. Once again, the peak pressure in the corners occurred after 80 μs to 100 μs and was lower in the top corners by approximately 25 % to 30 %. Interestingly, although venting had minimal effect on the mid-point pressure-time histories shown in Figure 16, adding venting reduced the magnitude of the peak pressure in the target plate corner nearest the vented side by approximately 10% while having no influence on the corners by the wall.

After 160 μs, the pressures had reflected from the ULD walls and returned to the centre of the ULD box and some pressure continued to vent from the open side. Much lower pressures were evident in the ULD in the later time phases (200 to 400 μs) although the internal pressure reflections continued as in the fully confined case. The predicted double vented pressure evolution was very similar to the single vented simulations, except that the peak target plate corner pressures were reduced by approximately 10 % on both sides (adjacent to both vents).

Concluding comments

Experiments were successfully performed on 1:6 scaled LD-3 to ascertain the influence of confinement and venting on the response of a deformable aluminium target plate situated at the diagonal face of the structure. The unconfined tests included transient measurement of the mid-line displacement using high-speed stereo imaging techniques. The unconfined tests showed good repeatability in the profile shape, peak displacement and features of the displacement-time history. The simulations showed that the confined detonations (regardless of venting type) caused peak pressures on the target plate that were three times greater than the unconfined detonations. The fully confined detonations also produced multiple reverberations of pressure within the structure. Introducing venting had a slight effect on the decay of the peak pressure and reduced the late-time pressure reflections inside the LD-3.

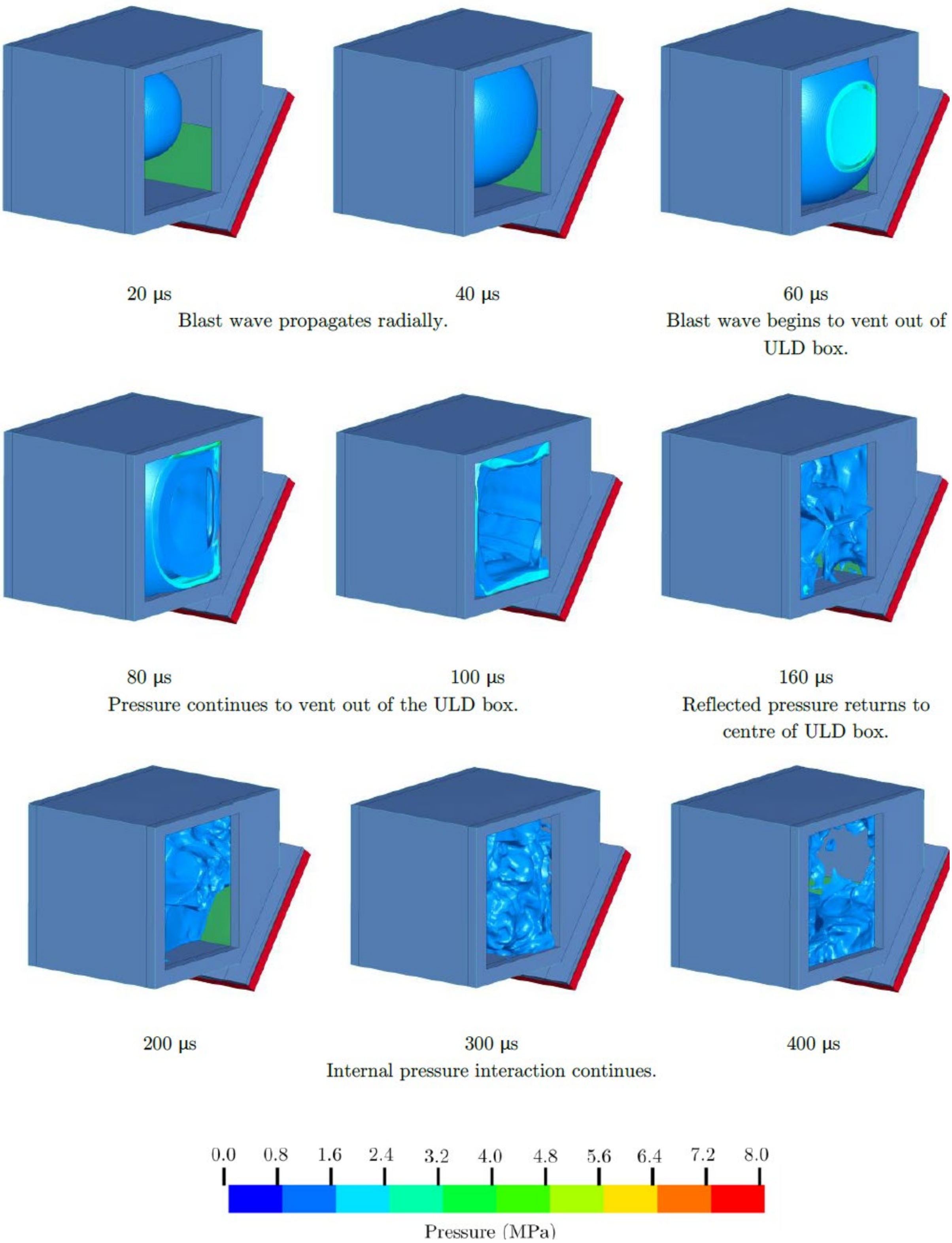

Figure 19: Simulated blast wave evolution for a 15g detonation for the single venting arrangement

The fully confined blast tests exhibited the highest permanent displacements and were the only tests to produce rupture of the target plate. Introducing single-sided or double-sided venting lowered the displacements (compared to full confinement with no venting). The influence of the side venting was slightly obscured in the experiments due to boundary pulling-in effects at higher charge masses, but the simulations showed that venting from two side was slightly more effective in reducing target plate deformation than single-sided venting.

The experiments and simulations have demonstrated the beneficial effect of venting: damage to the target plate was reduced and the later time pressure reflections within the structure were reduced. Practically speaking, this can be applied onboard aircraft by using LD-3 ULDs with canvas sides rather than solid ones. The LD-3 containers can be arranged in such a way that the blast loading vents from the open sides into the adjacent LD-3, allowing the pressure loading to propagate lengthwise along the aircraft body and away from the vulnerable parts of the primary framework immediately adjacent to the diagonal face of the LD3. It is expected these results will be helpful to blast engineers considering the threat of explosive detonations within aircraft luggage container bays.

Acknowledgements

The authors are grateful to the National Research Foundation (NRF) of South Africa for their financial support. Opinions expressed and conclusions arrived at, are those of the authors and are not necessarily to be attributed to the NRF.

References

1. Aerospaceweb.org, 2017. *Commercial Airline Bombing History*. Online article. http://www.aerospaceweb.org /question/planes/q0283.shtml

2. L. Dearden, 2017. *Isis plane attack: Egypt admits 'terrorists' downed Russian Metrojet flight from Sharam el Sheikh for first time*. Online news article. http://www.independent.co.uk/news/ world/africa/isis-plane-attack-egypt-terrorists-downed-russian-metrojet-flight-from-sharm-el-sheikh-islamic-state-a6893181.html

3. R. Kriel, P. Cruickshank, 2016. *'Sophisticated' laptop bomb on Somali plane got through X-ray machine*, Online article. http://edition.cnn.com/2016/02/11/africa/somalia-plane-bomb /index.html

4. D. Owen, 2006. *Air accident investigation* (3^{rd} ed.), Patrick Stevens Ltd, Somerset, UK.

5. Thompson, B 2019. *Unit load device ULD air container specifications*. Online article. https://incodocs.com/blog/unit-load-device-uld-air-container-specifications/

6. S. Emerson, B. Duffy, 1990. *The Fall of Pan-Am 103: Inside the Lockerbie Investigation*, G.P. Putnam's Sons, New York, US.

7. G.S. Langdon, W.J. Cantwell, 2020. The blast response of composite and fiber-metal laminate materials, In: *Polymer Composites in the aerospace industry (2nd ed.)* Eds: P Irving, C Soutis, Woodhead Publishing, UK.

8. W.A. Keenan, J.E. Tancreto, 1975. *Blast Environment from Fully and Partially Vented Explosions in Cubicles*, Report R828, Civil Eng Lab, Naval Construct Battal Cen, California.

9. C. Kingery, R. Schumacher, W. Ewing Jr, 1978, *Internal Pressure from Explosions in Suppressive Structures*, Report ARBRL-MR-02848, Aberdeen Proving Ground, Maryland.

10. C. Geretto, S. Chung Kim Yuen, G.N. Nurick, 2015. An Experimental Study of the Effects of Degrees of Confinement on the Response of Square Mild Steel Plates Subjected to Blast Loading, *Int J Impact Engng*, **79:**32–44.

11. J.A. Gatto, S. Krznaric, 1996. Pressure Loading on a Luggage Container due to an Internal Explosion, *Proc Conf Structures Under Shock and Impact*, pp. 61–77.

12. R.J. Curry, G.S. Langdon, 2017. Transient response of steel plates subjected to close proximity explosive detonations in air, *Int J Impact Eng*, 102:102-116.

13. G.S. Langdon, W.C. Lee, L.A. Louca, The influence of material type on the response of plates to air-blast loading, *Int J Impact Eng*, **78**:150-160, 2015.

14. G.S. Langdon, Y. Chi, G.N. Nurick, P. Haupt. Response of GLARE© panels to blast loading, *Eng Struct*, **31:**3116-3120, 2009.

15. Y.A. Çengel, M.A. Boules, 2011. *Thermodynamics: An Engineering Approach* (7th ed. SI), McGraw Hill, New York.

16. B.M. Dobratz, P.C. Crawford, 1985. *LLNL handbook of explosives: Properties of chemical explosives and explosive simulants*, Report UCRL-52997, Lawrence Livermore Natl Lab, University of California, US.

17. G.R. Johnson, W.H. Cook, 1983. A constitutive model and data for metals subjected to large strains, high strain rates and high temperatures, *Proc 7th Int Sympos Ballistics*, 541–547, Netherlands.

18. R. Smerd, S. Winkler, C. Salisbury, M. Worswick, D. Lloyd, M. Finn, 2005. High strain rate tensile testing of automotive aluminium alloy sheet, *Int J Impact Engng*, **32**:541–560.

19. ASM Handbook, 1993. Vol 2: Properties and Selection: Nonferrous Alloys and Special-Purpose Materials, *10th Edition Metals Handbook*, ASM International.

20. ASTM E8/E8M-16a, 2013. *Standard Test Methods for Tension Testing of Metallic Materials*, ASTM International.

21. S. Kriek 2019. *The effect of venting configuration on the blast response of an aircraft unit load device*, MSc dissertation, University of Cape Town.

22. H.L. Brode 1955. Numerical solution of spherical blast waves, *J Appl Phys* **26(6)**: 766.

23. C.A. Mills 1987. The design of concrete structure to resist explosions and weapon effects, *Proc 1st Int. Conf on concrete for hazard protections*, Edinburgh, UK, pp. 61-73.